

Article

Effect of Time on a Hierarchical Corn Skeleton-Like Composite of CoO@ZnO as Capacitive Electrode Material for High Specific Performance Supercapacitors

Yedluri Anil Kumar *  and Hee-Je Kim

School of Electrical Engineering, Pusan National University, Busandaehak-ro 63beon-gil, Geumjeong-gu, Busan 46241, Korea; heeje@pusan.ac.kr

* Correspondence: yedluri.anil@gmail.com or yedluri.anil@pusan.ac.kr;

Tel.: +82-10-3054-8401; Fax: +82-51-513-0212

Received: 25 October 2018; Accepted: 20 November 2018; Published: 25 November 2018



Abstract: CoO–ZnO-based composites have attracted considerable attention for the development of energy storage devices because of their multifunctional characterization and ease of integration with existing components. This paper reports the synthesis of CoO@ZnO (CZ) nanostructures on Ni foam by the chemical bath deposition (CBD) method for facile and eco-friendly supercapacitor applications. The formation of a CoO@ZnO electrode functioned with cobalt, zinc, nickel and oxygen groups was confirmed by X-ray diffraction (XRD) analysis, X-ray photoelectron spectroscopy (XPS), low and high-resolution scanning electron microscopy (SEM), and transmission electron microscopy (TEM) analysis. The as-synthesized hierarchical nanocorn skeleton-like structure of a CoO@ZnO-3h (CZ3h) electrode delivered a higher specific capacitance (C_s) of 1136 F/g at 3 A/g with outstanding cycling performance, showing 98.3% capacitance retention over 3000 cycles in an aqueous 2 M KOH electrolyte solution. This retention was significantly better than that of other prepared electrodes, such as CoO, ZnO, CoO@ZnO-1h (CZ1h), and CoO@ZnO-7h (CZ7h) (274 F/g, 383 F/g, 240 F/g and 537 F/g). This outstanding performance was attributed to the excellent surface morphology of CZ3h, which is responsible for the rapid electron/ion transfer between the electrolyte and the electrode surface area. The enhanced features of the CZ3h electrode highlight potential applications in high performance supercapacitors, solar cells, photocatalysis, and electrocatalysis.

Keywords: nanorod structure; nanocorn structure; hierarchical nanocorn skeleton-like structure; energy storage devices

1. Introduction

In recent years, with the increasing energy and power demands of the modern world, the continuous depletion of fossil energy and the continuous growth of the global economy has prompted considerable interest in the generation of renewable, clean and efficient energy (particularly in terms of the management, storage, and production of this precious energy) [1–4]. Among the electrical energy storage, ultra-capacitors have fascinated researchers and received enormous industrial attention because of their high charge–discharge current capability, high power density, very high efficiency, stable cycling performance, environmentally friendly nature and extensive temperature range compared to fuel cells [5]. Batteries have higher energy densities than traditional capacitors and conventional dielectric capacitors [6,7]. Therefore, major research has been directed towards the progression of supercapacitors with minimal sacrifice of the very high energy density and long cycling stability [8,9].

Supercapacitors are used widely in high power applications such as portable electronic devices, renewable energy storage devices, and hybrid electric vehicles [10]. Currently, the research into supercapacitors has focused mainly on the specific energy of supercapacitors and electrode materials and their micro- or nano-morphology [11]. In addition, continuous research has been concerned with designing long cycling performance electrode materials with stability, electrolyte and assembly technology [12–14]. Hence, the study of electrode materials has become a field of intense research activity [15].

Supercapacitors can be classified into two categories based on the energy storage mechanism: capacitors made typically from metal oxides or hydroxides and electric double layer capacitors (EDLCs) [16,17]. In EDLCs, carbon-based materials are commonly used in supercapacitor electrodes owing to their high power density, low cost, controllable porosity, and ease of process ability [18]. On the other hand, the relatively low energy density and volumetric capacitance has limited their efficient use for higher potential supercapacitor applications [19–21]. Some carbon-based materials, such as activated carbon and carbon nanotubes, were employed as electrode-based materials [22]. Nevertheless, in recent years, extensive attention has been paid to the surface area of the electrode [23]. In terms of capacitance, transition materials can have better capacitive performance than carbon-based EDLC electrodes, resulting from the interface, and they are thus categorized as supercapacitors. Capacitive materials contain metal oxides and sulfides, particularly metal oxide materials with higher specific capacitance, such as CoO, MnO₂, Fe₂O₃, and Co₃O₄ [24]. They have been considered promising anode materials compared to other capacitor materials and show more stable performance than carbon materials, which can result in excellent electrochemical capacitances as they can provide various oxidation states for capable faradic reactions [25]. Among those metal oxides, CoO is an ideal supercapacitor electrode material that has been shown to be promising for various applications due to its high redox reactivity, good electric conduction, low cost, high theoretic capacitance and ecofriendliness [26]. Moreover, CoO suffers from rapid capacity decay due to large volume expansion, limited ion transport kinetics and poor conductivity, cycling stability, and rate performances.

To overcome this problem, binary metal oxides show good electrochemical performance because they provide multiple redox reactions and have very high electrical conductivity. After the reaction, the two oxide interfaces formed exhibit new and interesting properties due to diffusion phenomena and proximity, which have become important in the nanoscale range. Binary metal oxide materials delivered excellent capacitances compared to single metal oxides because of their beneficial oxidation states and good electrical conductivity [27]. Among these metal oxides, ZnO has been described to be a good electrode potential material for Electrochemical capacitors (ECs) because of its simple fabrication, ecofriendliness and higher catalytic activity, as well as its high theoretical capacitance, mechanical stability, and high chemical stability. More surprisingly, ZnO/CoO exhibits good performance with superior reversible capacity and cycling stability compared to ZnCo₂O₄ [28]. The electrode material CoO@ZnO has been associated with the synergetic effects of the different components. Moreover, the hierarchical corn skeleton possesses the most closely-packed geometry, which allows for good electrical conductivity and a large surface area suitable for a high-performance faradic reaction. It is expected that the synergistic combination of these two materials (CoO and ZnO) could pave the way to enhanced electrochemical properties. More recently, Cai et al. described ZnO@Co₃O₄ core/shell heterostructures using facile hydrothermal synthesis. In contrast, the performance of metal oxide based materials is still lower. Nevertheless, it is a big challenge to develop metal oxides with different nanostructures and raise the potential of flexible electrochemical capacitors [29]. It is estimated that the similar CoO@ZnO should be an excellent electrode material.

In this study, CoO and ZnO electrodes were prepared and CoO@ZnO-1h (CZ1h), CoO@ZnO-3h (CZ3h) and CoO@ZnO-7h (CZ7h) electrodes were fabricated on Ni foam via a simple and inexpensive chemical bath deposition method (CBD) for supercapacitor applications. First, for optimization, the CoO nanorods were deposited uniformly on the as-prepared ZnO corn skeleton surface, such as CZ1h, CZ3h and CZ7h electrodes via the CBD method. The unique interconnected hierarchical

corn skeleton nanostructure of the CZ3h material resulted in an improved active electrode/electrolyte interface as well as a higher active material efficiency that facilitated ion and electron transfer for electrochemical reactions. Some studies indicated that hierarchical mixed oxides, i.e., cobalt and zinc oxide nanostructures, exhibit a large surface area as well as better electrical conductivity by producing hydroxyl groups and oxygen vacancies for the faradic reaction [30]. Under optimized conditions, the as-prepared CZ1h and CZ7h electrodes exhibited specific capacitance (240 F/g and 537 F/g at 3 A/g, respectively). On the other hand, the nanorod structure of the CoO electrode and corn skeleton-like ZnO electrode exhibited good specific capacitance (274 F/g and 383 F/g at 3 A/g, respectively). The hierarchical corn skeleton of the CZ3h electrode delivered a high specific capacitance of 1136 F/g at 3 A/g and a considerably long cycling lifetime, showing 98.3% capacitance retention after 3000 cycles. In this study, electrochemical measurements indicated that the hierarchical corn skeleton of CZ3h has remarkable electrochemical capacitance with good electrical conductivity and long lifetime cycling stability. The methodologies, through well-designed combinations and synthesized methods executed in this work, are applicable for the development of energy storage devices with ideal supercapacitor behavior and extraordinary electrochemical performance.

2. Experimental Methods

2.1. Chemicals and Materials

All of the reagents used in this study were of analytical grade and used without further purification. Analytical grade chemical reagents, zinc nitrate ($\text{Zn}(\text{NO}_3)_2$ (Chemical Abstracts Service (CAS) Number 13778-30-8)), hexamethylenetetramine ($(\text{CH}_2)_6\text{N}_4$ (Chemical Abstracts Service (CAS) Number 100-97-0)), cobalt acetate ($\text{C}_4\text{H}_6\text{CoO}_4$ (Chemical Abstracts Service (CAS) Number 71-48-7)), urea ($\text{CH}_4\text{N}_2\text{O}$ (Chemical Abstracts Service (CAS) Number 57-13-6)), acetic acid (CH_3COOH (Chemical Abstracts Service (CAS) Number 64-19-7)), and potassium hydroxide (KOH (Chemical Abstracts Service (CAS) Number 1310-58-3)) were purchased from Sigma Aldrich chemicals.

2.2. Preparation of ZnO and CoO on Nickel Foam

In a typical synthesis, pieces of Ni foam were cleaned carefully with a 1 M HCl solution for 30 min and dialyzed for a week to remove acids and ions. This was followed by a rinse in acetone, absolute ethanol, and deionized (DI) water in an ultrasonic bath for 20 min. A 50 mL precursor solution was prepared with 0.03 M of zinc nitrate and 0.04 M of hexamethylenetetramine (HMTA) with magnetic stirring for 30 min. The resulting light pink solution was transferred to a 50 mL beaker and the cleaned Ni foam substrates were immersed vertically into the reaction solution. Subsequently, the beaker was kept in an oven at 100 °C for 20 h. The loaded nickel foam precursor was washed carefully with absolute ethanol and DI water and kept in an oven at 100 °C for 1 h. Finally, the obtained product annealing the precursor at 350 °C for 3 h in a furnace to improve the crystallinity. A pure CoO electrode was also prepared using the same experimental method with the relevant chemicals without the addition of ZnO.

2.3. Preparation of CZ Composite Nanostructure

To synthesize CZ samples, 0.05 M cobalt acetate, 0.4 M acetic acid, and 0.04 M urea were dispersed in 50 mL of DI water with magnetic stirring for 30 min. The pink solution was transformed to a 50 mL beaker and the as-prepared ZnO electrode of Ni foam was immersed vertically into the solution and then kept in an electric oven at 100 °C for optimization of various timings, such as 1 h, 3 h and 7 h, to obtain the active electrodes. The reaction was allowed to cool to room temperature. The coating on the Ni foam was removed from the oven and rinsed carefully with absolute ethanol and DI water and maintained at 100 °C for 6 h in an oven.

2.4. Characterization

The products of the crystal structure and phase purity were characterized by powder X-ray diffraction (XRD, D8 ADVANCE, Tokyo, Japan). The morphology and microstructure of the synthesized products and elemental maps were characterized by scanning electron microscopy (SEM, s-2400, Hitachi, Tokyo, Japan) equipped with energy-dispersive X-ray spectroscopy (EDX). Amplitude-contrast transmission electron microscopy (TEM) was used to obtain information on the surface morphology and size. X-ray photoelectron spectroscopy (XPS) by VG scientific ESCALAB250 was used to study the elemental arrangement of the prepared materials.

2.5. Electrochemical Characterization

Cyclic voltammetry (CV) was carried out using a BioLogiSP150 electrochemical workstation instrument at various scan rates that ranged from 2 mVs⁻¹ to 6 mVs⁻¹ at a potential window of 0 V to 0.4 V. The galvanostatic charge–discharge (GCD) tests were conducted using chronopotentiometry at current densities from 3 A/g to 7 A/g at potentials ranging from 0 V to 0.4 V. The three-electrode cells were tested in a 2 M KOH aqueous solution as the electrolyte. The CZ electrodes on nickel foam were investigated directly as the working electrode, while a saturated Ag/AgCl electrode and a Pt wire were used as the reference and counter electrodes, respectively. Electrochemical impedance spectroscopy (EIS) measurements were taken over a frequency region between 0.100 Hz to 100 KHz at the open circuit potential with an alternating current (AC) potential amplitude of 5 mV. The energy density (E , Wh kg⁻¹), power density (P , W kg⁻¹), and specific capacitance (C_s , Fg⁻¹) were measured from the GCD curves using the equations:

$$E = \frac{C_s \times (\Delta V^2)}{2} \quad (1)$$

$$P = \frac{E}{t} \quad (2)$$

$$C_s = \frac{I \times t}{m \times V} \quad (3)$$

where I is the discharge current, t is the discharge time, V is the potential window and m is the mass of the active electrode, respectively.

3. Results and Discussion

The growth procedures of CoO, ZnO, CZ1h, CZ3h and CZ7h electrodes on Ni foam are illustrated in Figure 1.

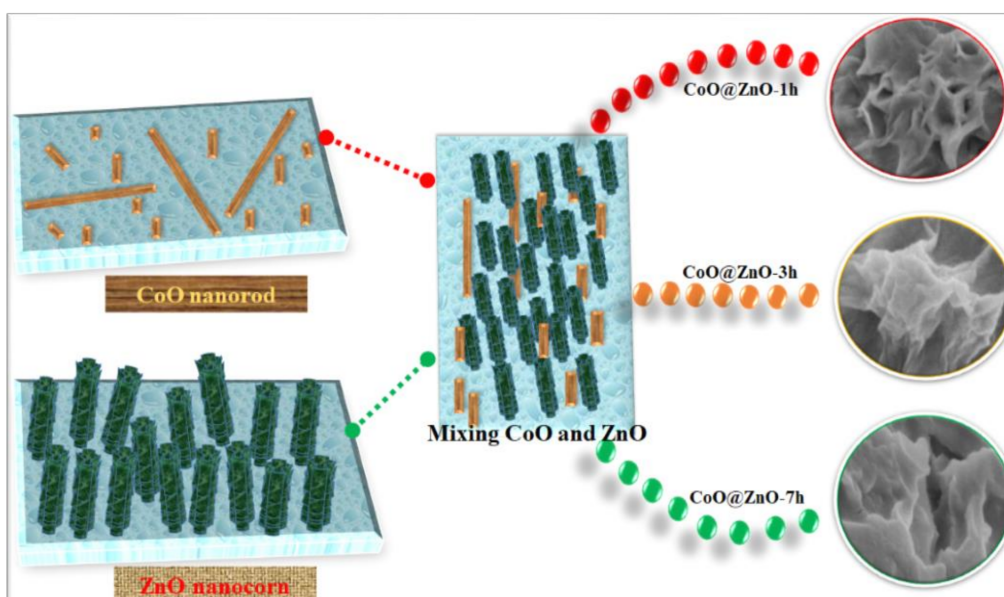


Figure 1. Illustration of the synthesis process of various nanostructures of CoO and ZnO and the effect of time on CZ composite electrodes on the Ni foam.

Characterization and Electrochemical Performance of Active Electrodes

The surface morphology, size and surface structures of the as-prepared electrodes, such as CoO and ZnO, were examined by low and high magnification Field emission scanning electron microscopy (FE-SEM) and Energy-dispersive x-ray spectrometer (EDS), as shown in Figure 2a–h.

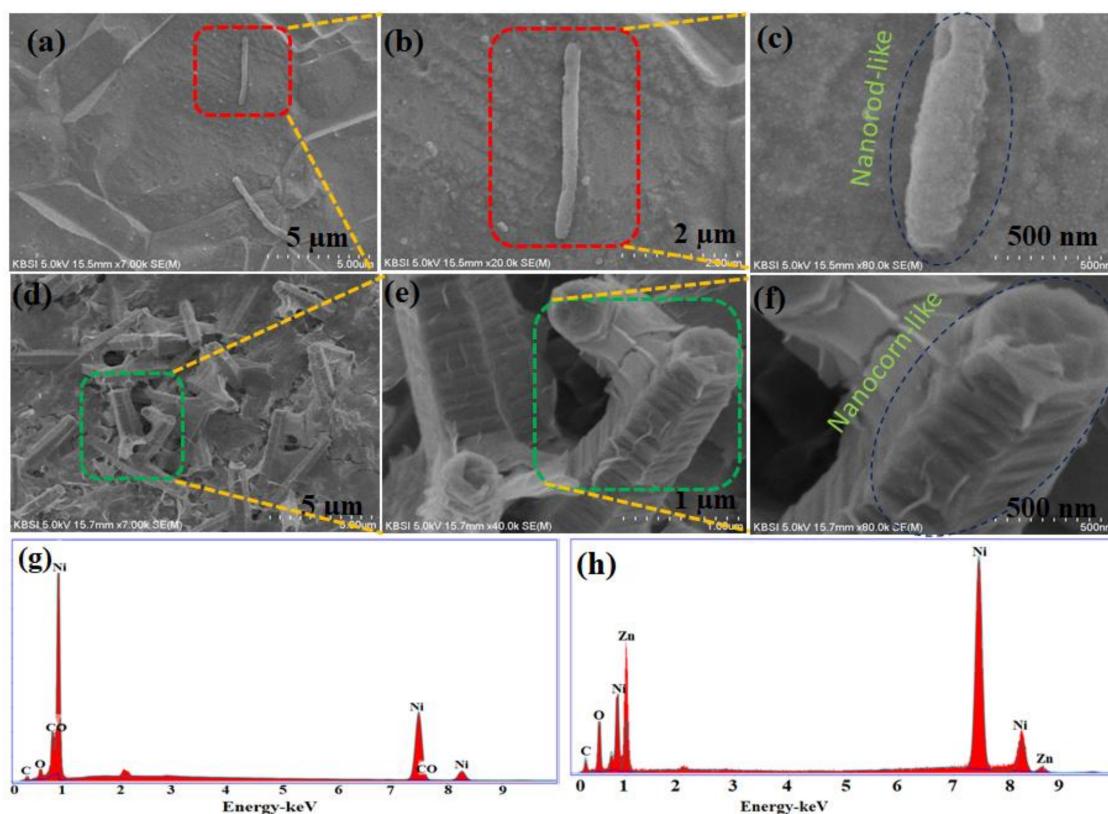
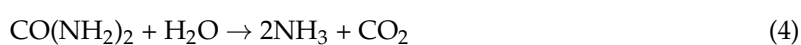
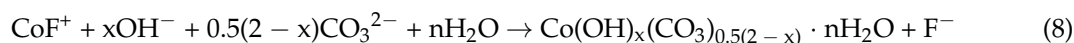


Figure 2. Low and high-magnification Field emission-scanning electron microscopy (SEM) images of the (a–c) CoO nanorod structures and (d–f) ZnO nanocorn structures and the energy-dispersive X-ray spectroscopy (EDX) pattern of CoO and ZnO (g,h) nanostructures on Ni foam.

Figure 2a–c presents SEM images of the CoO electrode on Ni foam by chemical bath deposition, indicating immature nanorods with different sizes and morphologies. Figure 2a,b shows low-resolution images of the CoO electrode. Different sized particles and the irregular morphology of the nanorod-like structure resulted in a smaller surface area of the electrode due to rapid nucleation. Figure 2c shows a high-resolution image of the CoO electrode showing a clear nanorod structure, indicating poor adhesion and a small surface area. Figure 2d–f presents low-resolution images of ZnO. The ZnO electrode showed well preserved nanocorn morphology on the Ni foam and may expose a larger surface area for growth of the active electrode, as shown in Figure 2d,e. The high-resolution SEM image of the ZnO electrode revealed the unique structure of a nanocorn morphology providing suitable diffusion channels for interactions with the electrolyte for the charge storage mechanism on the electrode surface (Figure 2f). Moreover, Figure 2f shows a high magnification of ZnO to illustrate the well-ordered nanocorn morphology on nickel foam. The high magnification SEM images (Figure 2f) show that ZnO consists of well-defined interconnected corn-shaped subunits with a size of around 200–500 nm and a thickness of around 20–30 nm. In addition, a large number of small pores with interconnected corn-like nanocorn structures were also observed. This type of unique interconnected nanocorn morphology provides suitable diffusion channels for the transport of the electrolyte and ensures efficient contact between the working electrode and electrolyte. Furthermore, EDX of CoO and ZnO (Figure 2g,h) confirmed the presence of Co, Zn, Ni, and O as the principal elemental components with no other impurities being obtained. EDX spectra of CZ1h and CZ7h (Figure S1a,b in the supporting information) confirmed the presence of Co, Zn, Ni and O as principal elemental components with no other impurities being obtained.

CZ was synthesized using the CBD method for various reaction times at 1 h, 3 h, and 7 h on Ni foam, such as CZ1h, CZ3h and CZ7h. Figure 3a–i shows low and high magnification FE-SEM images of the as-prepared samples. Figure 3a–c presents the CZ1h synthesized electrode on Ni foam. From Figure 3a,b, high magnification images of the active electrode revealed a nano-flake like structure that was formed by irregular connections with a low surface area and large pore sizes. In particular, Figure 3c indicates large pore sizes and less adhesion, making it difficult for ions or electrons to be transported within the electrode. Figure 3d–f presents the CZ3h synthesized electrode, indicating a well interconnected structure with a high surface area converted from the CZ1h electrode by the increased time. The nanostructure of CZ3h was comprised of CoO nanorods covered uniformly with the ZnO nanocorn surface area (Figure 3d,e). The high magnification SEM images of CZ3h confirmed that the synthesized composite has a non-uniform size which may be a result of the combination of particles with a corn skeleton-shape and the growth of unequal crystalline grains for the period of synthesis. Moreover, the CZ3h hierarchical nanocorn skeleton-like composites were closely connected to each other, which increased the number of electroactive sites for electrochemical reactions and formed a large surface area that can supply fast paths for the insertion and extraction of electrolyte ions, which is beneficial to the faraday reaction between the active material and electrolyte ions. Figure 3g–i shows the effects of increasing the time on the CZ7h electrode. As the annealing time was extended from 3 h to 7 h, the similar mesoporous structure of CZ7h was converted completely to disturbed nanoparticles with a weakened structure and large pores, indicating interrupted adjacent pores and a reduced surface area of the active electrode, as shown in Figure 3g,h. Figure 3i shows that the nanostructure is dispersed unevenly with voids among the particles on the surface of the active electrode. The corresponding chemical reactions occurred during the hydrothermal synthesis and are expressed using the following formulas:





The morphological features and structural information of the as-obtained samples of CoO, ZnO, and CZ1h, CZ3h and CZ7h were studied by transmission electron microscopy (TEM and High resolution-TEM), as shown in Figure S2a–f in the Supporting Information. Figure S2a–c in the Supporting Information shows a TEM image of the CoO electrode, which exhibits small sized nanorods and nanoparticle-like morphology. As shown in Figure S2a,b in the Supporting Information, irregular CoO nanoparticles were formed, resulting in a low surface area. Figure S2c in the Supporting Information shows thin CoO nanorods. Figure S2d–f in the Supporting Information presents low and high magnification TEM images of the ZnO nanocorn, showing good crystallinity with the observations from the SEM images. The low magnification TEM images of ZnO clearly showed the nanocorn nature by the nanosheet-like morphology with curling folded edges and obvious features, as shown in Figure S2d,e in the Supporting Information. Moreover, the obvious contrast shows (Figure S2f in the Supporting Information) black part and white part ligaments and indicates the mesoporous characteristics of the ZnO nanocorn-like structure. This is well consistent with the TEM observations, which were highly consistent with the SEM analysis.

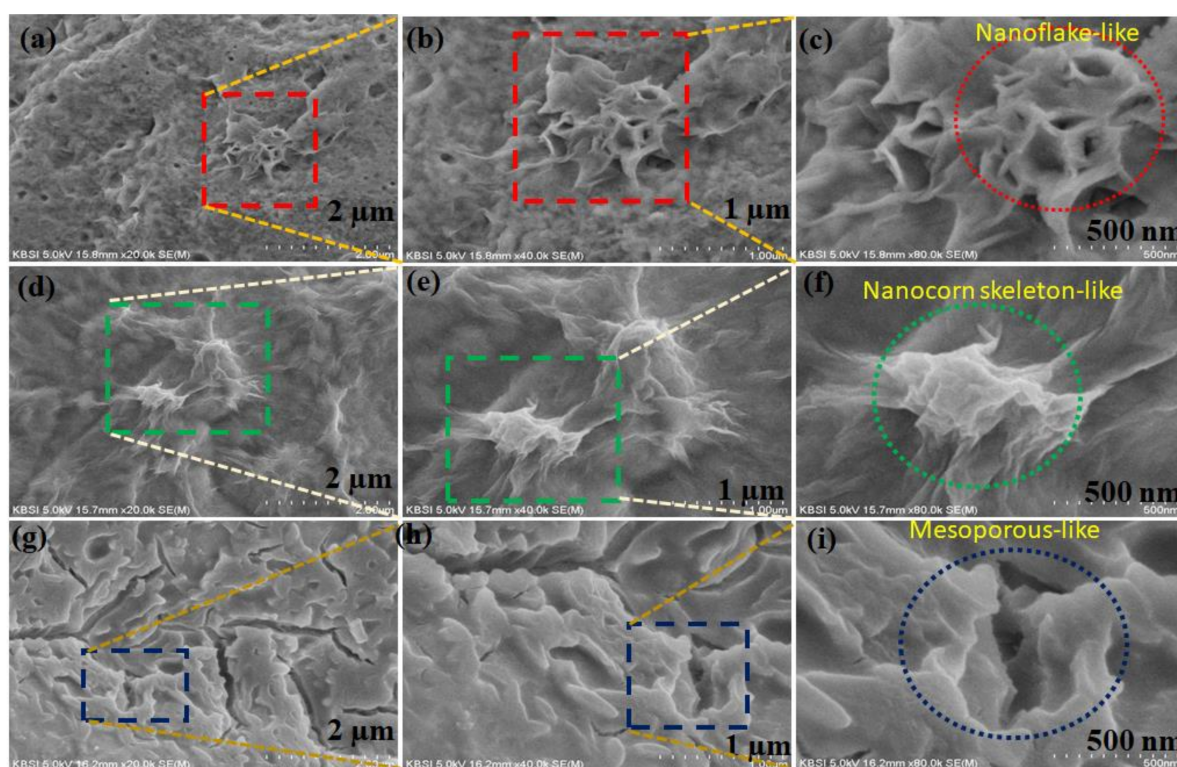


Figure 3. (a–c) SEM and FE-SEM images of CZ1h, (d–f) SEM and FE-SEM images of CZ3h and SEM and (g–i) FE-SEM images of CZ7h nanostructures.

Figure 4a presents low magnification images of the active electrode nanosheet-like structures. The CoO nanorods were evidently coated with ZnO corn straw nanostructures and formed a clear image, as shown in Figure 4b,c, indicating that this structure may shorten the ion diffusion length markedly for electrochemical reaction. On the other hand, EDS was performed on the CZ3h sample, as shown in Figure 4d, with active electrodes composed of Co, Zn, Ni, and O elements with no other impurities being obtained. Figure 4e,f presents different magnification images of the CZ1h electrode. The middle of the small thin layer sheet can be seen in Figure 4e, whereas the presence of CoO

nanoparticles on the edge of the ZnO nanosheet was observed clearly in Figure 4f. Figure 4g,h shows the TEM images of CZ7h at two different magnifications. Figure 4g shows a thin nanosheet, supporting the corresponding SEM images, which is also seen clearly in Figure 3h. Scanning transmission electron microscopy-energy dispersive x-ray spectroscopy (STEM-EDS) mapping has been used to investigate the elemental distribution in the CZ composite. Figure 4i,j shows the STEM image of the CZ3h hierarchical corn skeleton composite and its colored elemental mapping of Co and Zn, respectively. This result clearly proved the homogeneous distribution of Co and Zn in the CZ3h corn skeleton-like composite. Therefore, this hierarchical nanocorn skeleton-like (CZ3h) structure is beneficial for efficient and fast ion and electron transport to the surface of the active materials, which enhances the effective utilization of the active material.

The crystalline phase purity and composition of the as-prepared samples (CoO, ZnO, and CZ1h, CZ3h, and CZ7h) were examined by XRD as shown in Figure 5. In the XRD pattern of CoO, the XRD peaks at 21.8° , 36.84° , 37.8° , 43.3° , 44.81° , 49.7° , 63.29° , 75.2° and 78.40° 2θ were attributed to the (101), (003), (311), (400), (113), (400), (200), (622), and (311) planes, respectively. In CoO, all the XRD peaks were indexed using (Joint committee on powder diffraction standards (JCPDS) No. 48-1719) and related to the cubic phase. On the other hand, in the ZnO sample, the XRD peaks at 47.72° , 44.8° , 56.95° , 64.4° , and 68.2° 2θ were assigned to the (102), (400), (422), (220), and (112) planes of a well-crystallized hexagonal structure ZnO (JCPDS No. 36-1451). In the remaining samples of CZ1h, CZ3h, and CZ7h, the XRD peaks at 36.26° , 45° , 63.29° , 76.20° and 78.40° 2θ were assigned to the (311), (400), (511), (622), and (622) planes of a cubic spinel structure (JCPDS No. 23-1390), respectively. Moreover, the XRD pattern in Figure 5 confirmed the successful preparation of CoO and ZnO on Ni foam. No other peaks for impurities were observed, which confirms that the cobalt oxide precursor and zinc oxide precursor had been transformed completely to the CZ composite after chemical bath deposition at 300°C . In addition to these peaks, one strong peak in all samples at 51.9° 2θ was assigned to Ni foam. The specific surface area and pore size distribution are important factors for electroactive materials in supercapacitors. In order to evaluate the surface area properties of the as-synthesized CoO, ZnO, CZ1h, CZ3h and CZ7h electrodes, N_2 adsorption-desorption isotherms of “Brunauer-Emmett-Teller (BET) analysis” are shown in Figure 5b,c. Uniform distribution of CZ3h ensures a higher electrochemically active surface area and hence enhances the electrical conductivity. After analysis, CoO, ZnO, CZ1h and CZ7h were found to have minimal surface area and subsequently lower specific capacitance than CZ3h. The BET surface area and mean pore diameter of CoO, ZnO, CZ1h and CZ7h were found to be $22.6\text{ m}^2\text{ g}^{-1}$, $32.5\text{ m}^2\text{ g}^{-1}$, $27.3\text{ m}^2\text{ g}^{-1}$, $43.6\text{ m}^2\text{ g}^{-1}$ with an average pore size mostly below 10 nm, whereas CZ3h showed approximately $86.7\text{ m}^2\text{ g}^{-1}$ with an average pore size mostly below 20 nm. In addition, CZ3h showed enhanced pore size distribution and the pores were in the macroporous range. This mesoporous structure of the CZ3h electrode could enhance the specific surface area and the reaction sites at the interface of the electrolyte and electrode significantly.

XPS was also carried out to characterize the surface chemical composition and oxidation states of the chemical bonding of Co, Zn, Ni, and O on the surface of CoO, ZnO, and CZ1h, CZ3h, and CZ7h, and the results are presented in Figure 6. Figure 6b shows strong peaks for Zn 2p, Co 2p, Ni 2p and O 1s in the CZ3h survey spectrum. The high resolution Zn 2p spectrum shows the characteristic Zn $2p_{3/2}$ and Zn $2p_{1/2}$ peaks at 1022 eV and 1045 eV, respectively, confirming the presence of divalent Zn, as shown in Figure 6c. The strong peaks for Co 2p were typically deconvoluted into two peaks at 781.5 eV and 796.5 for Co $2p_{3/2}$ and Co $2p_{1/2}$, respectively, and two weak shake-up satellite peaks at 786.2 eV and 802.6 eV, as shown in Figure 6d [31,32]. The energy gap between the main peaks was approximately 15 eV, suggesting the presence of Co^{2+} and Co^{3+} . An energy gap between the main peaks and satellite peaks of around 6 eV would indicate divalent Co. Figure 6e shows the strong resolution X-ray photoelectron spectroscopy (XPS) of Ni 2p, which is typically separated into two strong peaks at 857.0 eV and 875.0 eV for Ni $2p_{3/2}$ and Ni $2p_{1/2}$, respectively, and its satellite peaks appear at 861.7 eV and 880.0 eV [33]. In addition, Figure 6f shows the O 1s spectrum with two

deconvoluted peaks at 531.0 eV and 529.8 eV, suggesting hydroxide ions and metal oxygen bonds in the sample [34–36].

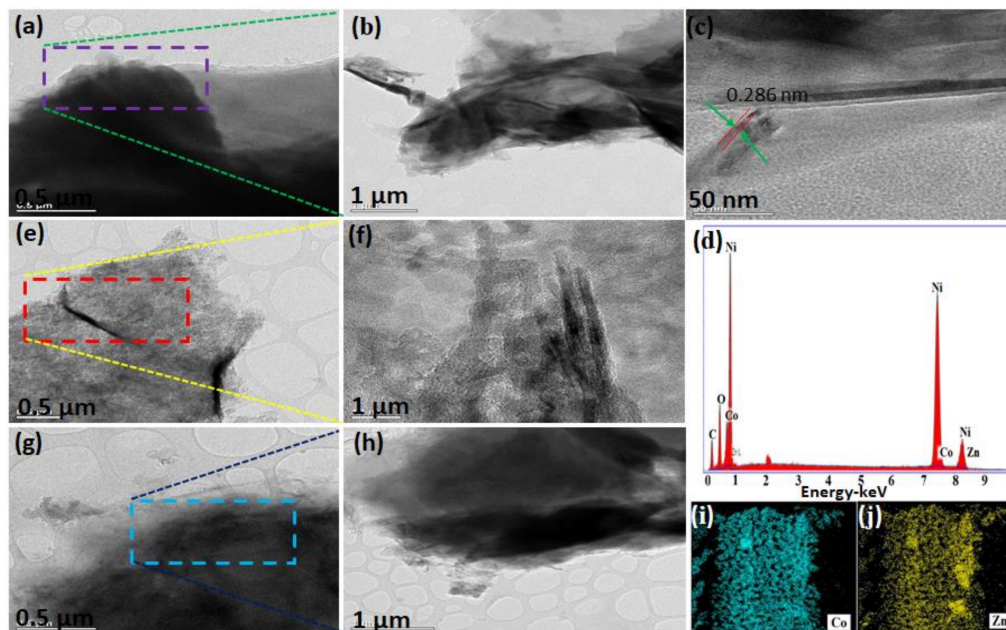


Figure 4. Transmission electron microscopy (TEM) and High resolution (HR-TEM) images for CZ3h, CZ1h and CZ7h composites. (a–c) presents low and high magnification TEM images of the CZ3h composite electrode and (d) Energy dispersive x-ray spectroscopy (EDS) spectrum, (e,f) CZ1h composite electrode, (g,h) CZ7h composite electrode and (i,j) elemental mapping images of Co and Zn.

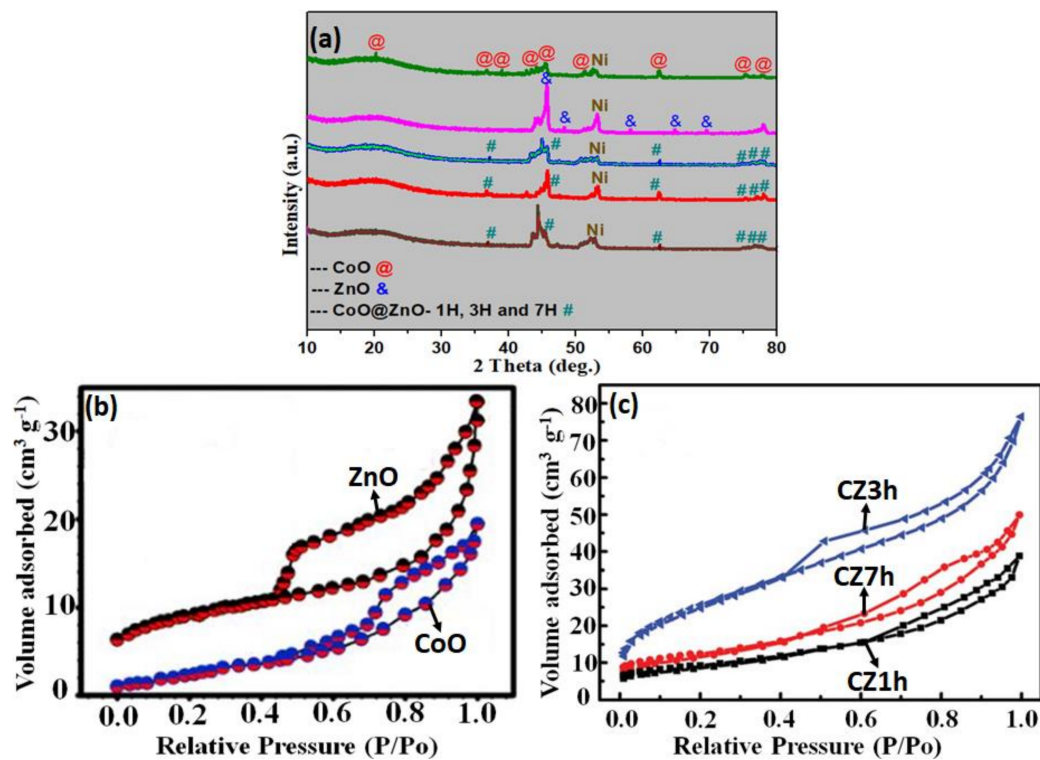


Figure 5. X-ray diffraction patterns (XRD) of all the samples. The Brunauer–Emmett–Teller (BET) surface area measured from nitrogen adsorption–desorption isotherms of (b) CoO and ZnO (c) CZ1h, CZ3h and CZ7h on Ni foam.

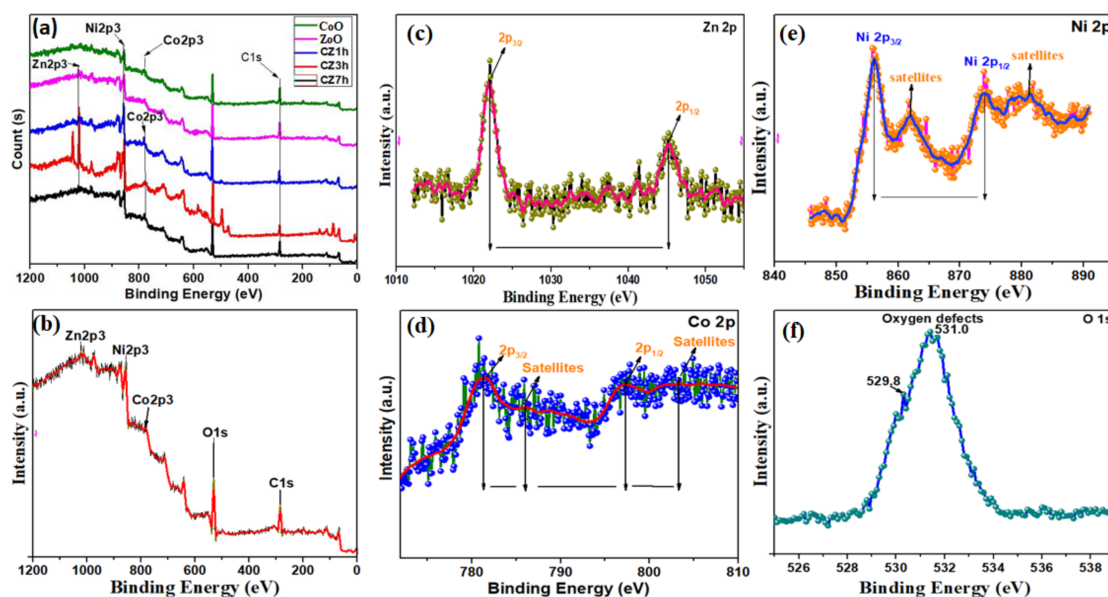


Figure 6. Shows the X-ray photoelectron spectroscopy (XPS) of (a) all samples and XPS spectra of CZ3h of (b) survey spectrum, (c) Zn 2p, (d) Co2p, (e) Ni 2p and (f) O 1s.

To examine the electrochemical behavior and supercapacitor properties of the as-prepared CoO, ZnO, and composites, the CZ1h, CZ3h, and CZ7h synthesized electrodes were first investigated in a three-electrode system (Figure 7). Figure 7a compares the CV curves of all the CoO, ZnO, CZ1h, CZ3h, and CZ7h electrodes in a 2 M KOH solution at 50 mV s^{-1} within a voltage window of 0 V to 0.4 V. The electrochemical performance of the CZ3h electrode was significantly higher than the remaining electrodes (CoO, ZnO, CZ1h, and CZ7h). The nanostructure of the CZ3h composite material shows great adhesion on the nickel foam substrate and a large surface area which produces more active sites for faradaic redox reactions and electron transport pathways, resulting in greatly enhanced electrochemical performance. Figure 7b shows the galvanostatic charge–discharge curves of all electrodes over 0 V to 0.4 V at 3 A/g. The prepared electrodes underwent the faradic redox reversible reactions. Remarkably, the CZ3h electrode exhibited a high specific capacitance, which is much larger than those for the CoO, ZnO, CZ1h, and CZ7h electrodes. The hierarchical corn skeleton structure of the CZ3h nanocomposite that was synthesized via a facile chemical bath deposition offers many remarkable advantages, such as efficient electrical contact between the nickel foam substrate and the electroactive materials and simplified electrode preparation, which act to improve capability and capacitance. Figure 7c shows the specific capacitance of the as-prepared samples calculated from the GCD curves at different current densities. For comparison, the specific capacitance of the CZ3h electrode exhibited 1136 F/g at 3 A/g, which is higher than the other electrodes. The strong synergistic effect of the CZ3h composite may contribute to the remarkable superior electrical performance compared with other electrodes such as CoO, ZnO, CZ1h and CZ7h. Figure 7d shows the CV profile of the individual CZ1h electrode. The shape of the CV curve remained the same even at a low scan rate of 2 mV s^{-1} up to a high scan rate of 100 mV s^{-1} and the GCD curves also maintained the same shape from current densities of 3 A/g to 7 A/g and exhibited a specific capacitance values of 240 F/g, 228 F/g, 214 F/g, 197 F/g and 190 F/g as shown in Figure 7e. The CV curves of the CZ3h composite electrode were investigated from 2–100 mV s^{-1} (Figure 7f). The CZ3h electrode showed a nanocorn morphology with an interconnected surface area, which is favorable for easy transportation in the electrochemical reaction. On the other hand, the GCD curves of the CZ3h electrode at various current densities (3 A/g to 7 A/g) exhibited a specific capacitance value of 1137 F/g, 1085 F/g, 892 F/g, 770 F/g and 675 F/g and are shown in Figure 7g. Construction of corn-skeleton structures with the combination of two different materials were shown to be a promising strategy to boost the greater electrochemical performance of metal oxides. Figure 7h shows the CV curves of the CZ7h electrode at various scan

rates. The current density increased with increasing scan rate, and all curves showed a unique shape. The GCD curves also maintained the same shape from current density values of 3 A/g to 7 A/g and exhibited specific capacitance values of 537 F/g, 512 F/g, 502 F/g, 492 F/g and 475 F/g, as shown in Figure 7i.

Figure S3a in the Supporting Information presents the CV profile of the CoO electrode, indicating the clear shape of the CV curve from 2–100 mV s^{-1} and GCD curves also maintained the same shape from current densities of 3 A/g to 7 A/g and exhibited specific capacitance values of 274 F/g, 255 F/g, 240 F/g, 217 F/g and 203 F/g (Figure S3b, Supporting Information), respectively. Figure S3c in the Supporting Information shows the CV curves of the ZnO electrode recorded at scan rates of 2–100 mV s^{-1} within the potential range from 0 to 0.4 V. The shape of the CV curve was the same even at a high scan rate of 100 mV s^{-1} . Figure S3d in the Supporting Information shows the charge–discharge curves at current densities (3 A/g to 7 A/g) and exhibited specific capacitance values of 383 F/g, 359 F/g, 312 F/g, 281 F/g and 273 F/g, respectively.

Ion diffusion and electron transfer in the electrode materials were examined. Figure 8a presents the Nyquist plot of all the electrodes over the frequency range of 0.100 Hz to 100 KHz. Figure 8a shows that the CZ3h electrode had a small semicircle in the high frequency range and a more vertical line in the low frequency range than the CoO, ZnO, CZ1h, and CZ7h electrodes, suggesting higher charge transfer between the active electrodes and the electrolyte. These very small circles are associated with rapid ion diffusion in the CZ3h electrode. These results show that combinations of the KOH aqueous electrolyte and the intrinsic resistance of the active electrode resulted in remarkable electrochemical performance of the CZ3h electrode.

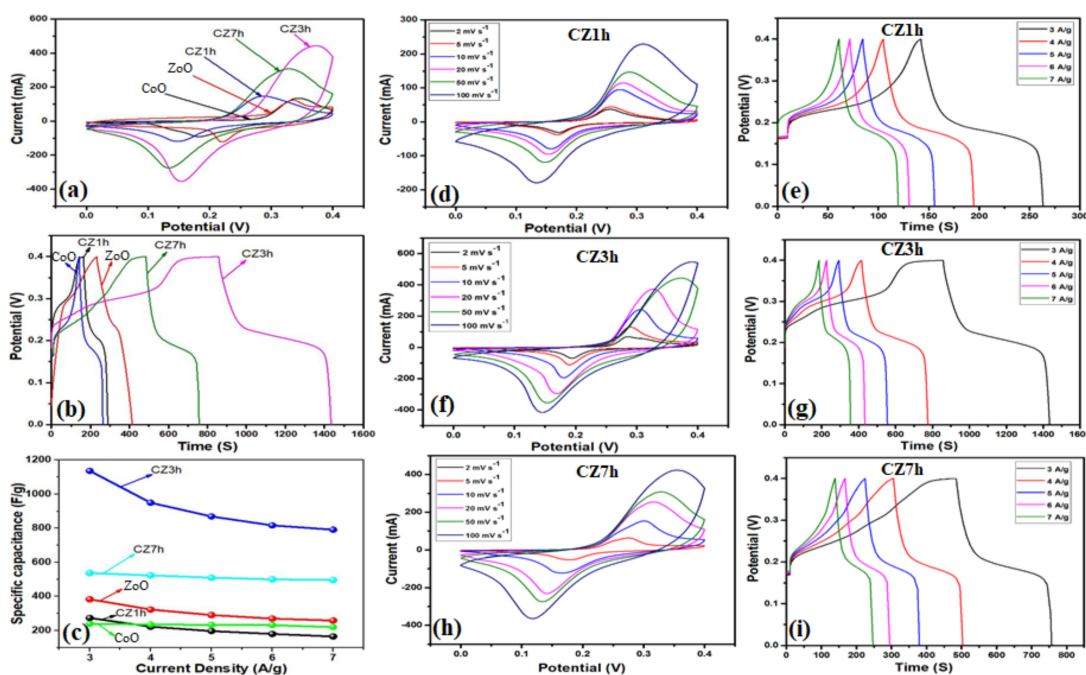


Figure 7. (a) Comparative cyclic voltammetry (CV) curves of the CoO, ZnO, CZ1h, CZ3h and CZ7h electrodes at a scan rate of 50 mV s^{-1} . (b) Comparative galvanostatic charge–discharge (GCD) curves of the CoO, ZnO, CZ1h, CZ3h and CZ7h electrodes at a current density of 3 A/g. (c) Specific capacitance vs. current density curve of the as-prepared electrodes, (d,e) CV curves and GCD curves of the CZ1h electrodes at various scan rates and current densities. (f,g) CV curves and GCD curves of the CZ3h electrodes at various scan rates and current densities. (h,i) CV curves and GCD curves of the CZ7h electrodes at various scan rates and current densities.

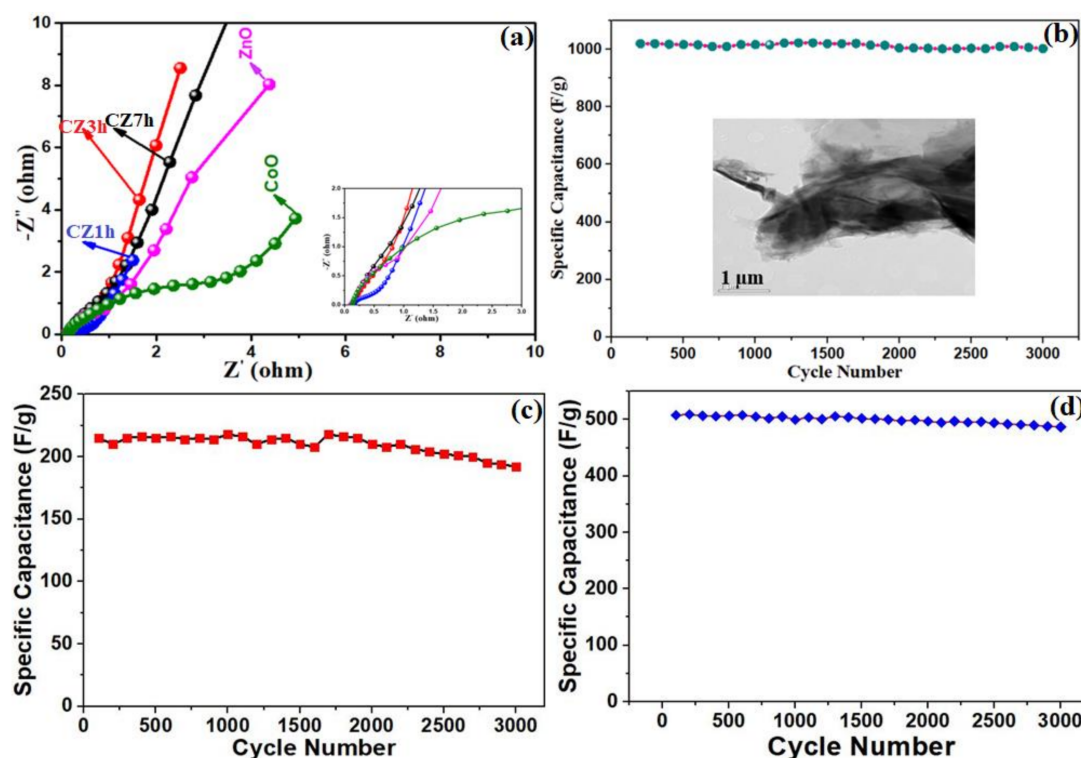


Figure 8. (a) Electrochemical impedance spectra (EIS) plots of the CoO, ZnO, CZ1h, CZ3h and CZ7h electrodes and (b–d) cycling stability performance of the CZ3h, CZ1h and CZ7h electrodes at 4 A/g for 3000 cycles.

A long-term cycle test was performed to examine the stability, which is an indispensable factor when determining the practical applicability of the CZ3h, CZ1h and CZ7h electrodes, as shown in Figure 8b–d. The cycling stability of the CZ3h, CZ1h and CZ7h electrodes were measured up to 3000 cycles by recording the GCD at a current density of 4 A/g in a three-electrode system. Figure 8b–d shows that the CZ3h electrode exhibits excellent capacitance that still retained 98.3% of the initial value after 3000 cycles, which was remarkably higher than those of CZ1h (83% initial value after 3000 cycles) and CZ7h (90.6% of the initial capacitance after 3000 cycles). This was attributed to the gradual penetration of the electrolyte into the interior of the electrode materials during cycling and the high structural stability of the electrode. Efficient electrical contact between the nickel foam substrate and the electroactive materials simplified electrode preparation, resulting in easy diffusion of the electrolyte and short ion diffusion pathways, thus leading to improved cycling stability and rate capability. To the best of our knowledge, these obtained output values for the CZ3h nanocomposite are the one of the greatest values and have good potential for supercapacitor applications compared to our previous reports and other composite materials (see Table 1).

Table 1. Comparison of various zinc- or cobalt oxide-based electrode materials and their electrochemical performances taken from recently published reports and the present work.

Electrode Materials	Electrolyte	Specific Capacitance at Current Density	Capacitance Retention (No. of Cycles)	Year, Ref.
Co ₃ O ₄ /ZnO	6 M KOH	415 F/g	93.2% (1000)	2016 (ref. [37])
ZnCo ₂ O ₄	6 M KOH	542.5 F/g	95.5% (2000)	2017 (ref. [38])
ZnCo ₂ O ₄	2 M KOH	776.2 F/g	84.3% (1500)	2017 (ref. [39])
Co ₃ O ₄ nanotube	6 M KOH	574 F/g	95% (1000)	2010 (ref. [40])
CNO–ZnO//ZnO	3 M KOH	125 F/g	92% (2000)	2017 (ref. [41])
ZnO nanoflakes	2 M KOH	260 F/g	73.33% (1000)	2018 (ref. [42])
Co ₃ O ₄ nanorods	6 M KOH	456 F/g	65% (500)	2009 (ref. [43])
ZnCo ₂ O ₄	2 M KOH	647.1 F/g	91.5% (2000)	2015 (ref. [44])
C@NiCo ₂ O ₄	6 M KOH	404 F/g	87.1% (1000)	2018 (ref. [45])
Co ₃ O ₄ /Graphene	6 M KOH	328 F/g	97.9% (2000)	2017 (ref. [46])
CZ3h	2 M KOH	1136 F/g	98.3% (3000)	This work

4. Conclusions

CoO, ZnO, CZ1h, CZ3h and CZ7h nanostructures were synthesized on Ni foam by an inexpensive and ecofriendly CBD method. Ni foam provides a higher surface area, excellent electrical conductivity, very high porosity, and sufficient functional groups to the material to enhance the electrochemical performance. Various electrochemical techniques were carried out to characterize the nanostructure, morphology, and structural properties of the working electrodes. The hierarchical interconnected corn skeleton of the CZ3h electrode allowed the electrolyte to penetrate directly, indicating a reduction in the ionic transfer resistance and thereby improving the working material surface area efficiency and electron transport. In a three-electrode system, the CZ3h active electrode exhibited a good specific capacitance (1136 F/g at a current density of 3 A/g). In contrast, the remaining electrodes (CoO, ZnO, CZ1h, and CZ7h) exhibited 274 F/g, 383 F/g, 240 F/g and 537 F/g at a current density of 3 A/g in the three-electrode system. Considering the encouraging electrochemical properties of the active electrodes device, it is strongly believed that hierarchical corn skeleton nanostructures will form part of new strategies for next generation energy storage devices.

Supplementary Materials: The following are available online at <http://www.mdpi.com/1996-1073/11/12/3285/s1>, Figure S1: EDX patterns of CZ1h and CZ7h electrodes (a,b) nanostructures on Ni foam, Figure S2: Shows the (a–c) TEM and HR-TEM images of CoO sample structures and (d–f) TEM and HR-TEM images of ZnO sample structures, Figure S3: (a,b) CV curves of the CoO and ZnO electrodes at various scan rates, (c,d) GCD curves of the CoO and ZnO electrodes at different current densities from 3 A/g to 7 A/g, Figure S4: Shows the X-ray photoelectron spectroscopy (XPS) of CZ1h and CZ7h electrodes of survey spectrums (a,b).

Author Contributions: Conceptualization, A.K.Y.; Formal analysis, H.J.K.; Investigation, A.K.Y. and H.J.K.; Methodology, A.K.Y.; Supervision, A.K.Y.; Writing—original draft, A.K.Y.; Writing—review and editing, A.K.Y.

Funding: This research received no external funding.

Acknowledgments: This work was financially supported by BK 21 PLUS, Creative Human Resource Development Program for IT Convergence (NRF-2015R1A4A1041584), Pusan National University, Busan, South Korea. We would like to thank KBSI, Busan for SEM, TEM, XRD, XPS and EDX analysis.

Conflicts of Interest: The authors declare no conflict of interest.

References

- Liao, J.; Zou, P.; Su, S.; Nairan, A.; Wang, Y.; Wu, D.; Wong, C.-P.; Kang, F.; Yang, C. Hierarchical nickel nanowire@NiCo₂S₄ nanowhisker composite arrays with a test-tube-brush-like structure for high-performance supercapacitors. *J. Mater. Chem. A* **2018**, *6*, 15284–15293. [CrossRef]
- Cai, D.; Huang, H.; Wang, D.; Liu, B.; Wang, L.; Liu, Y.; Li, Q. High performance supercapacitor electrode based on the unique ZnO@Co₃O₄ core/shell heterostructures on Nickel foam. *ACS Appl. Mater. Interfaces* **2014**, *6*, 15905–15912. [CrossRef] [PubMed]

3. Gopal, F.; Faraji, M. Preparation and electrochemical performances of nanoporous/cracked cobalt oxide layer for supercapacitors. *Appl. Phys. A* **2014**, *117*, 2087–20194. [[CrossRef](#)]
4. Kumar, Y.A.; Rao, S.S.; Punnose, D.; Tulasivarma, C.V.; Gopi, C.V.V.M.; Prabakar, K.; Kim, H.-J. Influence of solvents in the preparation of cobalt sulfide for supercapacitor. *R. Soc. Open Sci.* **2017**, *4*, 170427. [[CrossRef](#)] [[PubMed](#)]
5. Zhang, Y.; Ma, M.; Yang, J.; Su, H.; Huang, W.; Dong, X. Selective synthesis of hierarchical mesoporous spinal NiCo₂O₄ for high-performance supercapacitors. *Nanoscale* **2014**, *6*, 4303–4308. [[CrossRef](#)] [[PubMed](#)]
6. Chen, Z.; Wan, Z.; Yang, T.; Zhao, M.; Lv, X.; Wang, H.; Ren, X.; Mei, X. Preparation of nickel cobalt sulfide hollow nanocolloids with enhanced electrochemical property for supercapacitors applications. *Sci. Rep.* **2014**, *6*, 25151. [[CrossRef](#)] [[PubMed](#)]
7. Meng, X.; Sun, H.; Zhu, J.; Bi, H.; Han, Q.; Liu, X.; Wang, X. Graphene-based cobalt sulfide composite hydrogel with enhanced electrochemical properties for supercapacitors. *New J. Chem.* **2016**, *40*, 2843–2849. [[CrossRef](#)]
8. Kandalkar, S.G.; Gunjekar, J.L.; Lokhande, C.D. Chemical synthesis of cobalt oxide thin film electrode for supercapacitor application. *Appl. Surf. Sci.* **2008**, *254*, 5540–5544. [[CrossRef](#)]
9. Liu, S.; Mao, C.; Niu, Y.; Yi, F.; Hou, J.; Lu, S.; Jiang, J.; Xu, M.; Li, C. Facile synthesis of novel networked ultralong cobalt sulfide nanotubes and its application in supercapacitors. *ACS Appl. Mater. Interfaces* **2015**, *7*, 25568–25573. [[CrossRef](#)] [[PubMed](#)]
10. Yedluri, A.K.; Kim, H.-J. Wearable super-high specific performance supercapacitors using a honeycomb with folded silk-like composite of NiCo₂O₄ nanoplates decorated with NiMoO₄ honeycombs on nickel foam. *Dalton Trans.* **2018**, *47*, 15545–15554. [[CrossRef](#)] [[PubMed](#)]
11. Huang, K.-J.; Zhang, J.Z.; Shi, G.W.; Liu, Y.-M. One step hydrothermal synthesis of two-dimensional cobalt sulfide for high performance supercapacitors. *Mater. Lett.* **2014**, *131*, 45–48. [[CrossRef](#)]
12. Lin, J.-Y.; Chou, S.-W. Cathodic deposition of interlaced nanosheet-like cobalt sulfide films for high-performance supercapacitors. *RSC Adv.* **2013**, *3*, 2043–2048. [[CrossRef](#)]
13. Cheng, J.; Lu, Y.; Qiu, K.; Yan, H.; Xu, J.; Han, L.; Liu, X.; Luo, J.; Kim, J.K.; Luo, Y. Hierarchical core/shell NiCo₂O₄@NiCo₂O₄ Nanocactus arrays with dual-functionalities for high-performance supercapacitors and Li-ion batteries. *Sci. Rep.* **2015**, *5*, 12099. [[CrossRef](#)] [[PubMed](#)]
14. Yu, Z.; Tetard, L.; Zhai, L.; Thomas, J. Supercapacitor electrode materials: nanostructures from 0 to 3 dimensions. *Energy Environ. Sci.* **2015**, *8*, 702–730. [[CrossRef](#)]
15. Dong, W.; Wang, X.; Li, B.; Wang, L.; Chen, B.; Li, C.; Li, X.; Zhang, T.; Shi, Z. Hydrothermal synthesis and structure evolution of hierarchical cobalt sulfide nanostructures. *Dalton Trans.* **2011**, *40*, 243–248. [[CrossRef](#)] [[PubMed](#)]
16. Liu, R.; Ma, L.; Huang, S.; Mei, J.; Li, E.; Yuan, G. Large areal mass and high scalable and flexible cobalt Oxide/Graphene/Bacterial cellulose electrode for supercapacitors. *J. Phys. Chem. C* **2016**, *120*, 28480–28488. [[CrossRef](#)]
17. Tao, F.; Zhao, Y.-Q.; Zhang, G.-Q.; Li, H.-L. Electrochemical characterization on cobalt sulfide for electrochemical supercapacitors. *Electrochem. Commun.* **2007**, *9*, 1282–1287. [[CrossRef](#)]
18. Li, Z.; Han, J.; Fan, L.; Guo, R. Template-free synthesis of Ni₇S₆ hollow spheres with mesoporous shells for high performance supercapacitors. *CrystEngComm* **2015**, *17*, 1952–1958. [[CrossRef](#)]
19. Wang, X.; Zhao, S.-X.; Dong, L.; Lu, Q.-L.; Zhu, J.; Nan, C.-W. One-step synthesis of surface-enriched nickel cobalt sulfide nanoparticles on graphene for high-performance supercapacitors. *Energy Storage Mater.* **2017**, *6*, 180–187. [[CrossRef](#)]
20. Kumar, R.; Kim, H.-J.; Park, S.; Srivastava, A.; Oh, I.-k. Graphene-wrapped and cobalt oxide-intercalated hybrid for extremely durable super-capacitor with ultrahigh energy and power densities. *CARBON* **2014**, *79*, 192–202. [[CrossRef](#)]
21. Patil, D.S.; Pawar, S.A.; Shin, J.C. Core-shell structure of Co₃O₄@CdS for high performance electrochemical supercapacitor. *Chemical Engineering Journal.* **2018**, *335*, 693–702. [[CrossRef](#)]
22. Yedluri, A.K.; Kim, H.-J. Wearable super-high specific performance supercapacitors using a honeycomb with folded silk-like composite of NiCo₂O₄ nanoplates decorated with NiMoO₄ honeycombs on nickel foam. *Dalton Trans.* **2018**, *47*, 15545–15554. [[CrossRef](#)] [[PubMed](#)]

23. Singh, A.K.; Sarkar, K.K.; Mandal, K.; Khan, G.G. High-performance supercapacitor electrode based on cobalt oxide-manganese dioxide-nickel oxide ternary 1D hybrid nanotubes. *ACS Appl. Mater. Interfaces* **2016**, *8*, 20786–20792. [[CrossRef](#)] [[PubMed](#)]
24. Yao, M.; Hu, Z.; Liu, Y.; Liu, P. Design synthesis of hierarchical NiCo₂S₄@NiMoO₄ core/shell nanospheres for high-performance supercapacitors. *New J. Chem.* **2015**, *39*, 8430. [[CrossRef](#)]
25. Jiang, J.; Shi, W.; Song, S.; Hao, Q.; Fan, W.; Xia, X.; Zhang, X.; Wang, Q.; Liu, C.; Yan, D. Solvothermal synthesis and electrochemical performance in super-capacitor of Co₃O₄/C flower-like nanostructure. *J. Power Sources* **2014**, *248*, 1281–1289. [[CrossRef](#)]
26. Selvam, S.; Balamuralitharan, B.; Jegatheeswaran, S.; Kim, M.Y.; Karthick, S.N.; Raj, J.A.; Boomi, P.; Sundrarajan, M.; Prabakar, K.; Kim, H.J. Electrolyte-imprinted graphene oxide-chitosan chelate with copper crosslinked composite electrodes for intense cyclic-stable flexible supercapacitors. *J. Mater. Chem. A* **2017**, *5*, 1380–1386. [[CrossRef](#)]
27. Gu, Z.; Zhang, X. NiCo₂O₄@MnMoO₄ core-shell flowers for high performance supercapacitors. *J. Mater. Chem. A* **2016**, *4*, 8249. [[CrossRef](#)]
28. Bai, J.; Wang, K.; Feng, J.; Xiong, S. ZnO/CoO ZnCo₂O₄ Hierarchical Bipyramid Nanoframes: Morphology Control, Formation Mechanism, and Their Lithium Storage Properties. *ACS Appl. Mater. Interfaces* **2015**, *7*, 22848–22857. [[CrossRef](#)] [[PubMed](#)]
29. Yedluri, A.K.; Kim, H.-J. Wearable super-high specific performance supercapacitors using a honeycomb with folded silk-like composite of NiCo₂O₄ nanoplates decorated with NiMoO₄ honeycombs on nickel foam. *Dalton Trans.* **2018**, *47*, 15545–15554. [[CrossRef](#)] [[PubMed](#)]
30. Niu, H.; Zhou, D.; Yang, X.; Li, X.; Wang, Q.; Qu, F. Towards three-dimensional hierarchical ZnO nanofiber@Ni(OH)₂ nanoflake core-shell heterostructures for high-performance asymmetric supercapacitors. *J. Mater. Chem. A* **2015**, *3*, 18413. [[CrossRef](#)]
31. Du, J.; Zhou, G.; Zhang, H.; Cheng, C.; Ma, J.; Wei, W.; Chen, L.; Wang, T. Ultrathin porous NiCo₂O₄ nanosheet arrays on flexible carbon fabric for high-performance supercapacitors. *ACS Appl. Mater. Interfaces* **2013**, *5*, 7405–7409. [[CrossRef](#)] [[PubMed](#)]
32. Yuan, C.; Li, J.; Hou, L.; Zhang, X.; Shen, L.; Lou, X.W. Ultrathin mesoporous NiCo₂O₄ nanosheets supported on Ni foam as advanced electrodes for supercapacitors. *Adv. Funct. Mater.* **2012**, *22*, 4592–4597. [[CrossRef](#)]
33. Pujari, R.B.; Lokhande, A.C.; Kim, J.H.; Lokhande, C.D. Bath temperature controlled phase stability of hierarchical nanoflakes CoS₂ thin films for supercapacitor applications. *RSC Adv.* **2016**, *6*, 40593–40601. [[CrossRef](#)]
34. Xiao, X.; Han, B.; Chen, G.; Wang, L.; Wang, Y. Preparation and electrochemical performances of carbon sphere@ZnO core-shell nanocomposites for supercapacitor applications. *Sci. Rep.* **2017**, *7*, 40167. [[CrossRef](#)] [[PubMed](#)]
35. Zheng, Q.; Kvit, A.; Cai, Z.; Ma, Z.; Gong, Z. A free standing cellulose nanofibril-reduced graphene oxide-molybdenum oxynitride aerogel film electrode for all-solid-state supercapacitors with ultrahigh energy density. *J. Mater. Chem. A* **2017**, *5*, 12528–12541. [[CrossRef](#)]
36. Mahajan, H.; Bae, J.; Yun, K. Facile synthesis of ZnO-Au composites for high performance supercapacitors. *J. Alloys Compd.* **2018**, *758*, 131. [[CrossRef](#)]
37. Xu, J.; Liu, S.; Liu, Y. Co₃O₄/ZnO nanoheterostructure derived from core-shell ZIF-8@ZIF-67 for supercapacitors. *RSC Adv.* **2016**, *6*, 52137. [[CrossRef](#)]
38. Gai, Y.; Shang, Y.; Gong, L.; Su, L.; Hao, L.; Dong, F.; Li, J. A self-template synthesis of porous ZnCo₂O₄ microspheres for high-performance quasi-solid-state asymmetric supercapacitors. *RSC Adv.* **2017**, *7*, 1038–1044. [[CrossRef](#)]
39. Xu, L.; Zhao, Y.; Lian, J.; Xu, Y.; Bao, J.; Qiu, J.; Xu, L.; Xu, H.; Hua, M.; Li, H. Morphology controlled preparation of ZnCo₂O₄ nanostructures for asymmetric supercapacitor with ultrahigh energy density. *Energy* **2017**, *123*, 296–304. [[CrossRef](#)]
40. Mohapatra, D.; Parida, S.; Badrayyana, S.; Singh, B.K. High performance flexible asymmetric CNO-ZnO//ZnO supercapacitor with an operating voltage of 1.8V in aqueous medium. *Appl. Mater. Today* **2017**, *7*, 212–221. [[CrossRef](#)]
41. Xu, J.; Gao, L.; Cao, J.; Wang, W.; Chen, Z. Preparation and electrochemical capacitance of cobalt oxide (Co₃O₄) nanotubes as supercapacitor material. *Electrochim. Acta* **2010**, *56*, 732–736. [[CrossRef](#)]

42. Pant, B.; Park, M.; Ojha, G.P.; Park, J.; Kuk, Y.S.; Lee, E.J.; Kim, H.Y.; Park, S.J. carbon nanofibers wrapped with zinc oxide nanoflakes as promising electrode for supercapacitors. *J. Coll. Interface Sci.* **2018**, *522*, 40–47. [[CrossRef](#)] [[PubMed](#)]
43. Cui, L.; Li, J.; Zhang, X.G. Preparation and properties of Co_3O_4 nanorods as supercapacitor material. *J. Appl. Electrochem.* **2009**, *39*, 1871. [[CrossRef](#)]
44. Wang, Q.; Zhu, L.; Sun, L.; Liub, Y.; Jiao, L. Facile synthesis of hierarchical porous ZnCo_2O_4 microspheres for high-performance supercapacitors. *J. Mater. Chem. A* **2015**, *3*, 982. [[CrossRef](#)]
45. Li, W.; Yang, F.; Hu, Z.; Liu, Y. Template synthesis of $\text{C@NiCo}_2\text{O}_4$ hollow microsphere as electrode material for supercapacitor. *J. Alloys Compd.* **2018**, *749*, 305–312. [[CrossRef](#)]
46. Yang, M.H.; Choi, B.G. Preparation of Three-Dimensional Co_3O_4 /graphene Composite for High-Performance Supercapacitors. *Chem. Eng. Commun.* **2017**, *204*, 723–728. [[CrossRef](#)]



© 2018 by the authors. Licensee MDPI, Basel, Switzerland. This article is an open access article distributed under the terms and conditions of the Creative Commons Attribution (CC BY) license (<http://creativecommons.org/licenses/by/4.0/>).